Progress In Electromagnetics Research B, Vol. 32, 263–282, 2011

FRESNEL LENSES BASED ON NANO SHELL-SILVER COATED SILICA ARRAY FOR SOLAR CELLS APPLICATIONS

T. A. Elwi * **and H. M. Al-Rizzo**

Department of Systems Engineering, University of Arkansas at Little Rock, AR 72204, USA

Abstract—Fresnel lenses are low-cost optical elements used for focusing sunlight to solar panels to ensure operation under high-flux density. However, the conventional Fresnel lens has a relatively high material usage and hence contributes to additional efficiency degradation. Moreover, traditional design of Fresnel lenses introduces additional prismatic facets, due to deviations in manufacturing, which reflect the light toward the back focal spot, leading to additional losses. In this paper, Fresnel lenses based on finite arrays of Nano Shell-Silver Coated Silica (NSSCS) are proposed to overcome the aforementioned drawbacks from infrared regime through the visible band to the ultraviolet region. To identify reflection losses, material losses of the NSSCS array and rejection bands due to the NSSCS array arrangement, three unique electromagnetic (EM) approaches are invoked: Frequency Selective Surfaces (FSS) to determine reflection bands, Metamaterial (MTM) to specify material losses and Electromagnetic Band Gap (EBG) to locate the rejection band. The EM characteristics of the NSSCS array are evaluated for wavelengths ranging from 0.3 µm to 300 µm, using CST MicroWave Studio (CST MWS), which is based on the Finite Integration Technique (FIT). It is found that the NSSCS array exhibits excellent transmittance within two bands, one from 545 nm to 857 nm and the other from 444.5 nm to 480 nm, for angles ranging from 0° to 180° along the azimuth and elevation. The effective refractive index (n_{eff}) spectra showed that the NSSCS array does not provide a negative for its real (n_{eff}) part over the considered wavelength band. The imaginary part of (n_{eff}) value is found to be almost insignificant, between 0.857 µm to 1.714 µm and 316 nm to 414 nm and lossy elsewhere. In general, the NSSCS array shows no specific stop band over the considered frequency

Received 13 June 2011, Accepted 9 July 2011, Scheduled 19 July 2011

* Corresponding author: Taha A. Elwi (taelwi@ualr.edu).

region. Fresnel lenses based on a 9×9 NSSCS array configuration with planar, concave and convex profiles are presented in this paper. The beam width and power density of the emerged beams are evaluated at different wavelengths for different lens sizes. In general, it is found that the power density spectrum is largely dependent on the imagery part of n_{eff}. Nevertheless, the beam width decreases by increasing the lens size, while it decays for wavelengths longer than 500 nm. The concave and convex profiles are introduced to further enhance beam width. The effects of increasing the lens size from 9×9 to 11×11 on the beam width are reported for the concave and convex profiles. It is found that the concave design provides almost a constant beam width at 666.7 nm, 461.5 nm and 316 nm with changing array size, while the convex design does not. Characteristics of the emerged EM beams, in terms of beam waist, depth of focus and phase retardation, are evaluated based on Gaussian optic formalisms for the 9×9 NSSCS array. It is found that the beam waist and the depth of focus for the flat profile vary from 334.03 nm to 387.90 nm and 105.16 nm to 285.65 nm, respectively. The beam waist changes from 365.12 nm to 381.41 nm, while the depth of focus changes from 125.65 nm to 289.45 nm for the convex profile. Finally, the beam waist changes from 313.36 nm to 318.19 nm, and the depth of focus changes from 925.49 nm to 201.45 nm for the concave profile.

1. INTRODUCTION

The most important bench-parameter to assess the viability of solar energy, whether through thermal conversion or by photovoltaic technology, is the cost of electrical current generated per kilowatt hour [1]. To meet the urgent demand of reducing the cost of electricity generated from photovoltaic technologies, light trapping, anti-reflection coatings, silicon technology and thin-film technology have been invoked to reduce the material usage [2]. Moreover, the use of Fresnel lenses to focus energy in solar cell applications is still in the research phase [3]. Basically, a concentrator is an optical element that focuses the flux density of sunlight onto a small area of a solar panel. However, the concentrated flux and material losses may lead to a severe damage in solar cells due to excessive temperature rise that reduces their efficiency [3]. In this case, a cooling system should be added to the solar cells, which increases their cost. From a designer's point of view, a solar cell wafer with minimum material losses and passive cooling properties is the most desirable [3]. Lens array technology for Fresnel lens applications is one of the most promising candidates to overcome the increase in temperature and material losses

by reducing material usage and providing increased aperture spacing for heat dissipation [4]. These arrays can be constructed based on different optical materials, from bulk to nano-scale structures. For example, a metal slit array-based Fresnel lens was investigated in [5] to couple light into silicon nano-photonic waveguides. In [6], the authors provided an experimental demonstration for plasmonic lens-based nano-slits in an aluminum film in the visible range.

Recently, extensive studies have been reported on non-dispersive, bulk photonic crystals consisting of periodical cells embedded in an infinite homogenous medium [7–9]. The periodicity can be uniform or non-uniform based on 1-D, 2-D or 3-D structures. The interactions between EM waves and periodical crystals using traditional Maxwell's theory have been extended to the nano-scale for plasmonic structures [10–14].

The concept of EBG is a popular EM approach to analyze EM interactions with periodical macroscopic dielectric media [15, 16]. The most essential property of EBG is the existence of a frequency band in which EM propagation is forbidden. Characterizing the EM properties of EBG structures through their dispersion diagram and First Brillion Zone (FBZ) were reported in [17]. Furthermore, manipulating the spontaneous emission using EBG structures for efficient lasers, bipolar junction transistors and solar cells has been proposed in [18].

In another aspect, these periodical structures are referred to as MTM as originally envisioned by Victor Veselago [19] to create a sharp image out of a point source. John Pendry developed an analytical formulation for the perfect focusing [19]. In fact, the main difference between classical curved lenses and planar MTM lenses is that the latter does not have an optical axis and reconstitutes the near-field as well as the far-field of the source with a sub-wavelength resolution by virtue of resonant surface waves that are excited in the MTM. These lenses are considered almost perfect lenses since their spatial resolution is limited only by losses in the lenses' material.

Another group of structures referred to as Frequency Selective Surfaces (FSS) has recently attracted a great deal of research interest [20–22]. These structures possess a unique property called frequency selective property using an array of conducting patches or aperture elements in a metallic screen or on a dielectric substrate [21]. The transmission and reflection properties of these surfaces depend on the wavelength and may also depend on the polarization and angle of incidence.

In this paper, we investigate the optical performance of lenses based on finite planar, concave and convex profiles of 9×9 NSSCS arrays. The EM characteristics of the proposed NSSCS array lenses

are evaluated based on three unique approaches: EBG, MTM and FSS from 0.3 μm up to 300 μm. The proposed approach allows the designer to locate the band gap, quantify material losses and characterize the reflection properties with respect to the angle of incidence. The characteristics of the emerged EM beams, beam waist, depth of focus and phase retardation are evaluated using Gaussian optical formalism at 666.7 nm, 461.5 nm and 316 nm.

It is found that such structures are promising for solar cell applications since they can increase the optical beam focusing over certain wavelength bands when they are introduced on the top of the solar panels.

The rest of the paper is organized as follows. In Section 2, we present the material properties and geometrical configuration. In Section 3, we provide the simulation setups and results. In Section 4, we present the theoretical formulation and results based on optical concepts. Finally, in Section 5, we conclude the paper.

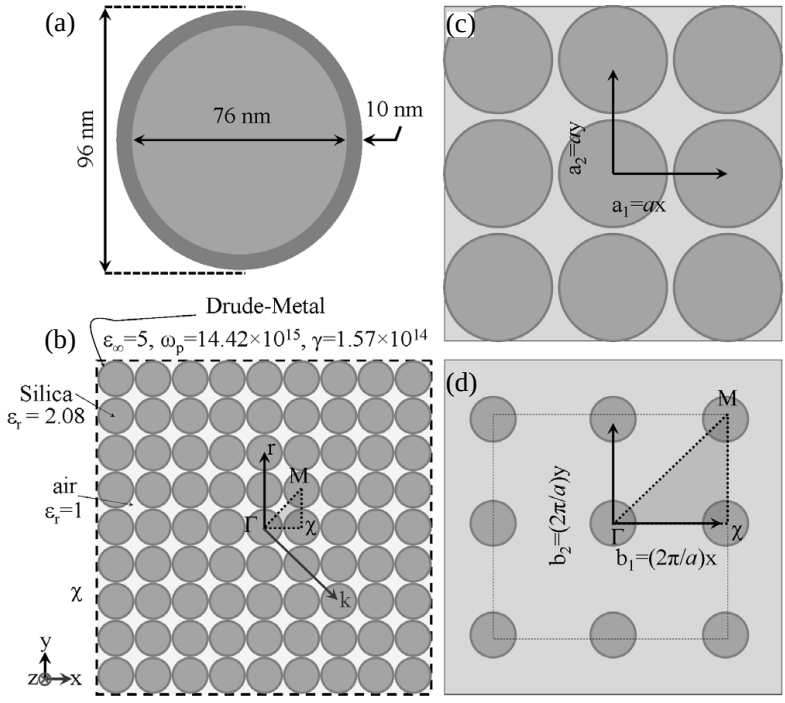

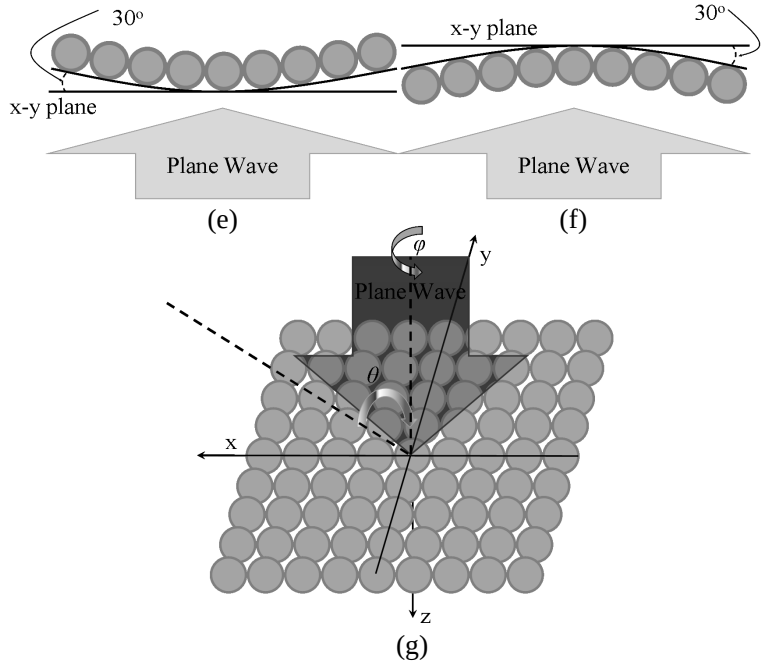

Figure 1. Geometrical details of (a) NSSCS unit cell, (b) the 9×9 NSSCS planar array, (c) real lattice for NSSCS array, (d) reciprocal lattice for NSSCS array, (e) convex NSSCS array, (f) concave NSSCS array and (g) 3-D sketch showing φ and θ directions.

2. GEOMETRICAL CONFIGURATION

An individual NSSCS is constructed from a spherical silica core coated with a spherical shell of metallodielectric silver nanostructures. In Fig. 1(a), the geometry of the unit cell is presented using the dimensions reported in [12]. We started with a finite planar array of 9×9 unit cells as presented in Fig. 1(b). The array of the NSSCS is in the x-y plane in vacuum. The planar array is excited with a plane wave of unity amplitude. The electric field is polarized along the x-axis and the propagation direction is along the z-axis. In Fig. 1(b), the array represents a photonic crystal of square lattice with an arbitrary vector $\mathbf{r}$, where $\mathbf{r}$ is the primitive unit vector. The highlighted triangle (Γ, M, χ), where Γ, χ and M follow the reciprocal lattice notation of a natural crystal, represents the irreducible Brillion zone of the square lattice centered at the origin Γ with an arbitrary wave vector $\mathbf{k}$. The NSSCS is a sphere of silica with a non-dispersive

permittivity ε_r coated with a silver shell [12]. Silver, however, is a noble metal that becomes dispersive dielectric at optical frequencies. The dispersion behavior of silver follows the classical Drude model at optical frequencies, $\varepsilon = \varepsilon_\infty + \{\omega_p^2/(\omega^2 - i\omega\gamma)\}$, where ε_∞ is the permittivity at infinite frequency, ω_p is the plasma frequency and γ is the collision frequency [11]. The periodical repetition of the planar array of NSSCS with a lattice distance of a (defined as the distance between two adjacent unit cells) along the x- and y-axes can be represented in both real and reciprocal lattice as shown in Figs. 1(c) and 1(d), respectively. In the square lattice of the NSSCS array, the NSSCS unit cell is repeated with a distance of $a_1 = ax$ along the x-axis and $a_2 = ay$ along y-axis as seen in Fig. 1(c). The primitive axes of the reciprocal lattice of the NSSCS array are calculated as $b_1 = (2\pi/a)x$ and $b_2 = (2\pi/a)y$ as shown in Fig. 1(d). The real lattice is presented by the 2-D structure of NSSCS as shown Fig. 1(c) and the FBZ is represented by the dashed box shown in Fig. 1(d). The three directions of the primitive lattice vector represented by $\Gamma\chi$, χ-M and M-Γ are given by b_1, b_2 and b_3, and are shown in Fig. 1(d).

In this paper, we will also consider finite concave and convex arrays of 9×9 unit cells as depicted in Figs. 1(e) and 1(f). Furthermore, the EM performance of the 2-D NSSCS array will be reported versus the local position of the EM source with respect to the azimuth (φ) and elevation (θ) angles as depicted in Fig. 1(g).

3. NUMERICAL RESULTS

3.1. NSSCS Array as FSS Structures

The transmission spectra of the infinite array of NSSCS are investigated at different incident angles ($\varphi = 0^\circ$ to 180° and $\theta = 0^\circ$ to 180°) at a step of 18° in both directions. A single NSSCS is surrounded by an air box. The boundaries of the four-sided faces are selected as Periodic Boundary Conditions (PBC). The other two sides are assigned as Open Boundaries (OBC) in the direction perpendicular to the direction of propagation to realize Floquet Modes (FLM). The two FLM ports are assigned in opposite directions as shown in Fig. 2.

The transmission spectra shown in Fig. 3 clearly demonstrate that the change in the transmission spectra of the NSSCS array is almost insignificant with respect to the angle of incident along θ and φ; this reveals that the accepted power is constant with changing the angle of incident. This property results in an increased coupling efficiency, which is desirable for solar cell applications [24]. The NSSCS array shows excellent transmittance, below -10 dB, for wavelength bands from 0.545 μm to 0.857 μm and from 444.5 nm to 480 nm.

3.2. NSSCS Array as MTM Structures

A unit cell of NSSCS is positioned along the center of a fictitious waveguide as shown in Fig. 4 to retrieve $n_{eff}(\omega)$ using the simulated scattering parameters as reported in [3]. The two ports of TEM-like

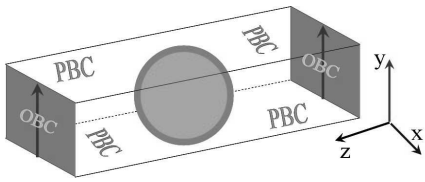

Figure 2. The boundary conditions set-up of FSS problem. The black arrows at the OBC show the FLM.

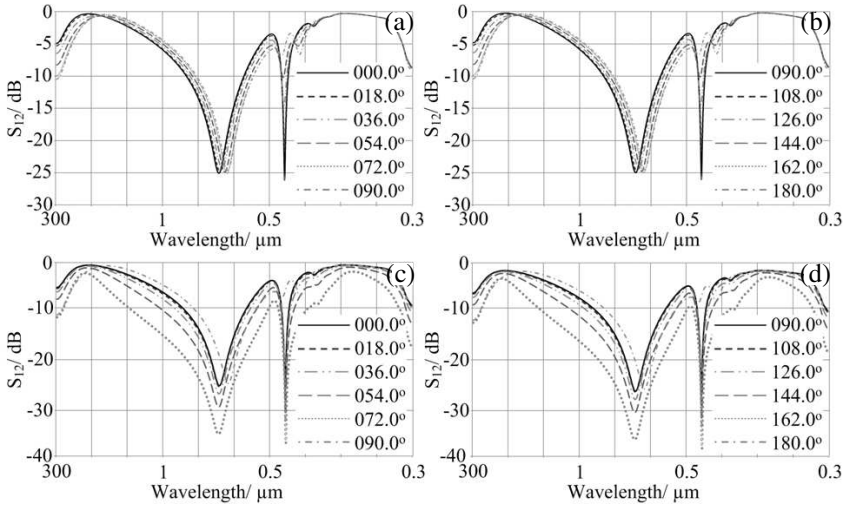

Figure 3. Transmission spectra versus angle of incident; (a) and (b) θ changing from 0° to 180° and (c) and (d) φ changing from 0° to 180°.

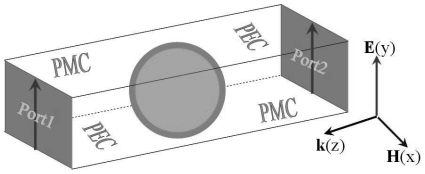

Figure 4. 3D view for the waveguide model used to characterize the NSSCS array.

modes are shown in Fig. 4. The top and bottom sides are assigned as perfect electric conductors (PECs), and the other two sides are assigned as perfect magnetic conductors (PMCs). The dimension of the NSSCS unit cell with respect to the wavelength ($\lambda = 600\,\text{nm}$) is $\lambda/6.25$. The NSSCS unit cells are separated by $\lambda/6.25$. Fig. 5 shows the magnitude and phase of the scattering parameters. Fig. 6 shows the $n_{eff}(\omega)$ of the NSSCS array, which is computed from the scattering parameters. The magnitude of the real part of $n_{eff}(\omega)$ is less than one at three different bands, the shaded areas in Fig. 6, that mimic the behavior of MTM.

The results shown in Fig. 6 reveal that the NSSCS array does not exhibit negative refractive index over the considered wavelength band. However, the NSSCS shows significant losses over certain wavelength bands, which in turn lead to a reduction in the power density of the emerged EM beams from the NSSCS array when it used as a Fresnel lens as will be shown later.

The real part of n_{eff} depicted in Fig. 6 shows an almost perfect lens consisting of an infinite array of NSSCS with a focal length of f_ℓ. However, in the case of a finite array, the array size affects the numerical aperture, which affects f_ℓ, as given by $n_\ell(r) = n_{euc}(\omega) - d/2f_\ell$ where $n_{euc}(\omega) = \sqrt{\varepsilon_{euc}(\omega)}$ is the effective refractive index of the individual unit cell of the NSSCS having $\varepsilon_{euc}(\omega)$ which is a function of ε_{Ag} and ε_{silica}, d is the effective width of the NSSCS lens and $n_\ell(r)$

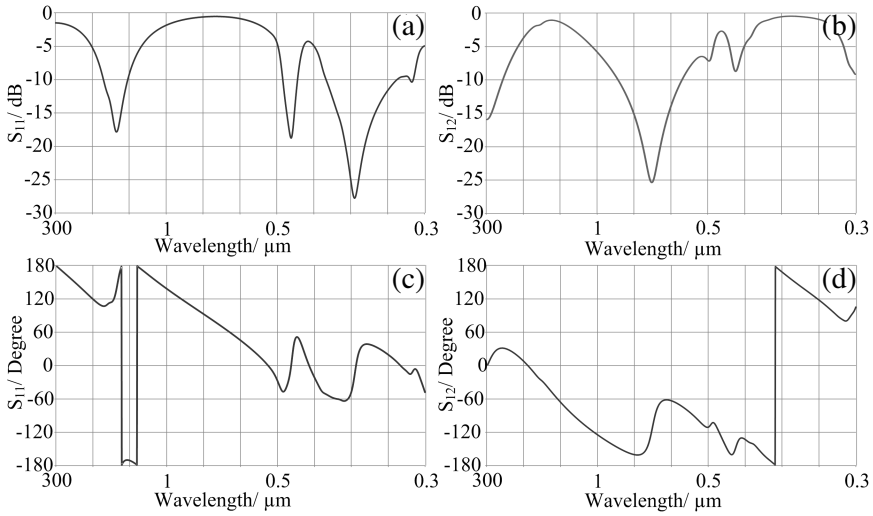

Figure 5. Scattering parameters of the infinite planar array of NSSCS; (a) S_{11} and (b) S_{12} magnitudes, (c) S_{11} and (d) S_{12} phases.

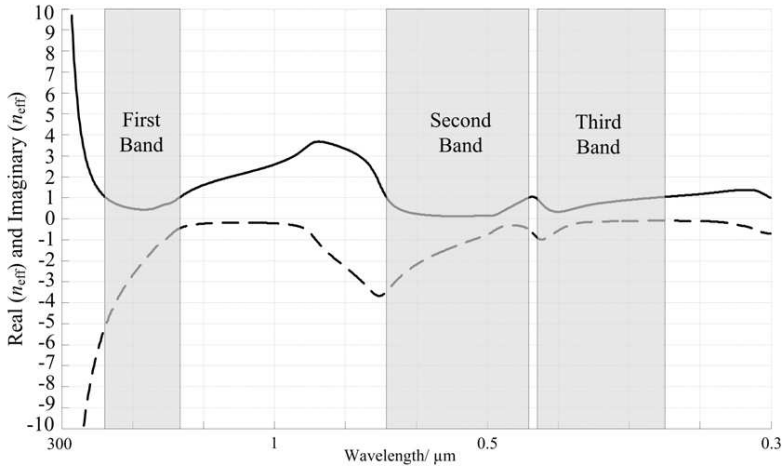

Figure 6. Effective refractive index $n_{eff}(\omega)$.

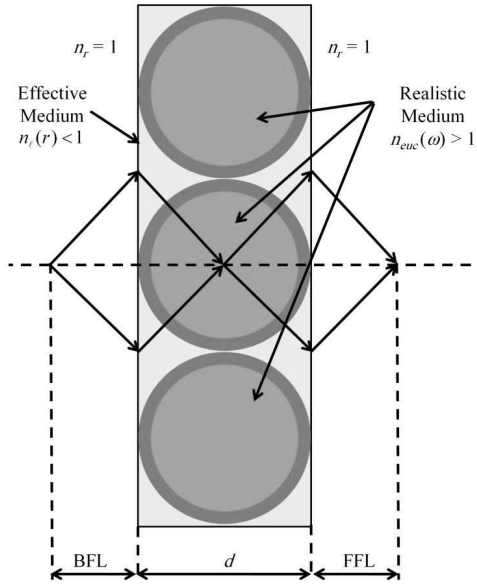

Figure 7. Planar MTM lens.

is refractive index of the effective medium of the lens as a function of both array dimensions and $n_{eff}(\omega)$. The front focal length (FFL) and back focal length (BFL) equal to f_ℓ as shown in Fig. 7 with other geometrical details.

3.3. NSSCS Array as EBG Structures

The dispersion diagram can be extracted using the Brillouin-zone theory reported in [25]. The numerical setup shown in Fig. 8 is used to evaluate the dispersion diagram within the FBZ along the x-direction which is denoted as phase-1 that varies from 0°–180° with constant phase of 0° at y-direction. Next, by phase-y is changed from 0°–180° while keeping phase-x at 180° to determine the dispersion diagram along the y-direction. The last direction along x- and y-phases is found by simultaneously varying their phases from 180°–0° In Fig. 8, PBC and PML refer to Periodic Boundary Condition and Perfect Matching Layer, respectively. In Fig. 9 the dispersion diagram for the NSSCS array is shown, normalized to the angular structure resonance $\omega_o = \pi c_o/a$. The NSSCS array shows no stop band over the wavelength range under consideration. This is advantageous for the proposed Fresnel lens as light propagation within the solar cell devices is not being rejected.

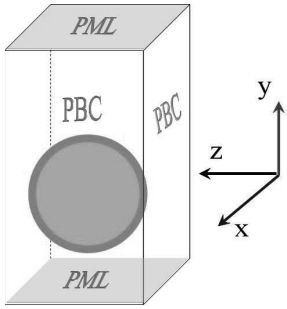

Figure 8. The numerical set-up for evaluating the dispersion diagram.

4. PERFORMANCE OF THE PROPOSED LENSES

4.1. Parametric Study of the NSSCS Array

The effects of the number of the unit cells on the beam emerging from the proposed lens are reported within a range from 1 to 9 with step 2. The power density of the beam emerging from the proposed lens versus wavelength from 0.3 µm to 6 µm is presented in Fig. 10. The power density is integrated over a sphere of radius 1 m surrounding the lens at the center. It is found that the power density increases with increasing the number of the NSSCS unit cells. The power density spectrum fluctuates in a fashion that is similar to the imaginary part of $n_{eff}(\omega)$ shown in Fig. 6.

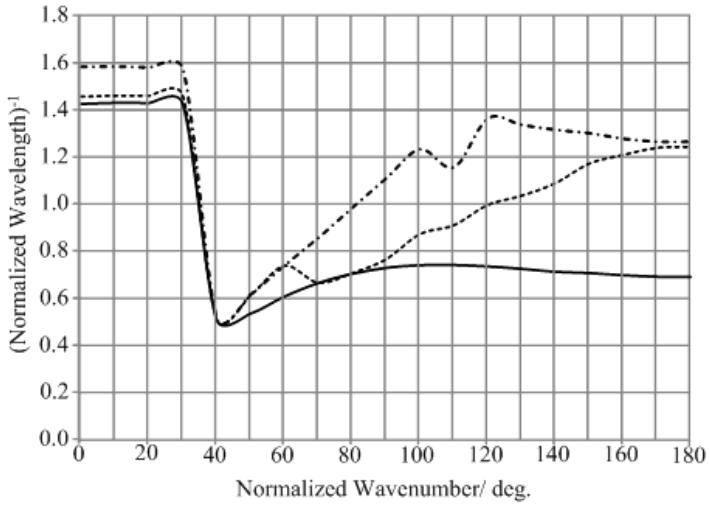

Figure 9. The dispersion relation diagram for planar NSSCS array.

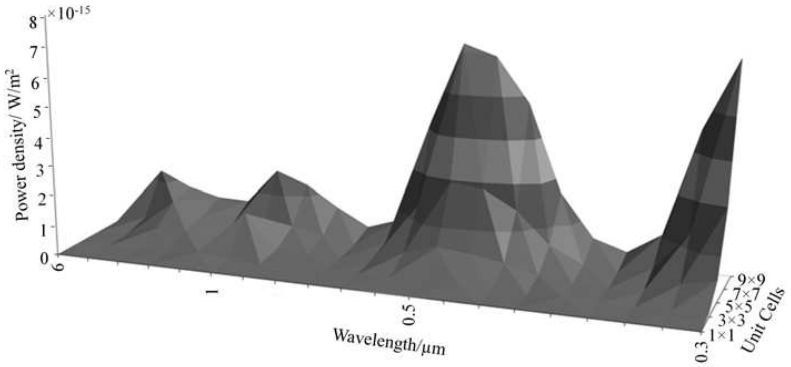

Figure 10. Power density spectrum for the proposed lens versus the number of unit cells.

Additionally, change in power patterns along the bore-sight direction versus the number of NSSCS unit cells is reported. Due to the abundance of configurations and repetitions of the NSSCS unit cells, the power density pattern normalized to 0 dB is shown in Fig. 11 for wavelengths ranging from 0.3 μm to 3 μm for the 1×1 and 9×9 arrays. As seen in Figs. 11(a) and 11(b), the direction of the bore-sight changes from 180° to 0° with wavelength change from 0.3 μm to 0.5 μm, while it starts to become more focused from 333 nm to 429 nm, then diverges at 0.3 μm. Therefore, it appears in the case of 1×1 array that the

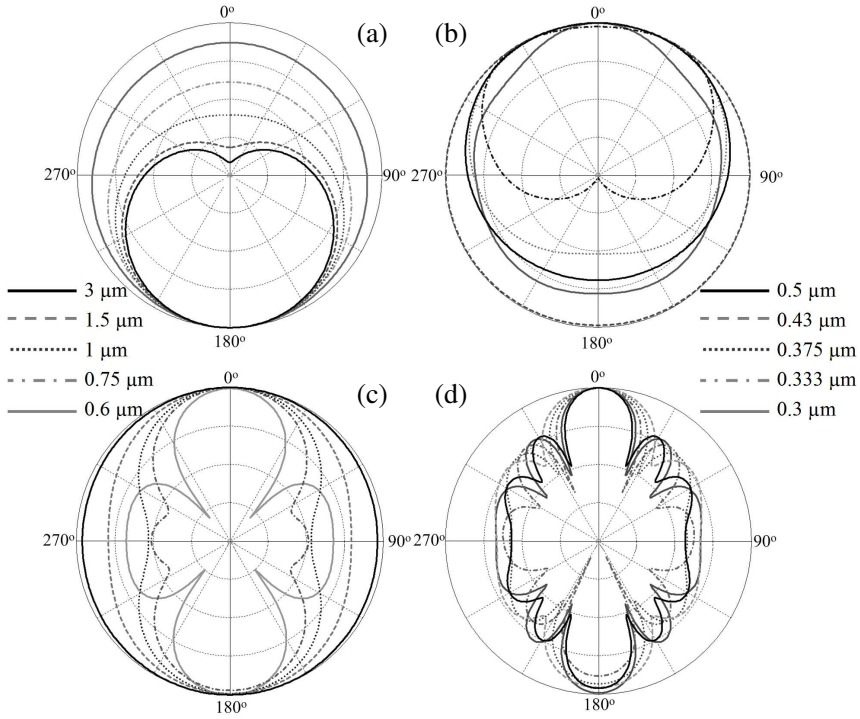

Figure 11. The normalized power density pattern from the EBG lens at $\varphi = 90°$ with changing wavelength from 0.3 μm up to 3 μm within 10 steps; (a) and (b) 1×1, (c) and (d) 9×9.

beam is more affected with changing wavelength than the 9×9 array. Moreover, the 9×9 array can provide almost a Gaussian beam with minimum beam width through reducing the chromatic aberrations. From results presented in Figs. 11(c) and 11(d), the power density pattern shows some changes from 0.6 μm to 3 μm, while, no change has been observed from 0.3 μm to 0.5 μm. Finally, it is found that the FFL equals the BFL in the case of the 9×9 array as can be seen in Figs. 11(c) and 11(d), while it is not the same case with the 1×1 array as shown in Figs. 11(a) and 11(b). Therefore, we concluded that the 9×9 array exhibits almost a perfect lens where FFL = BFL, at which the lens has no optical axis.

4.2. Performance of the Curved NSSCS Lenses

The power density patterns emerging from the 9×9 curved lens for wavelengths of 666.7 nm, 461.5 nm and 316 nm are calculated over a

surrounding sphere with three different radii: 0.75 m, 1 m and 1.25 m are shown in Fig. 12. The convex and concave NSSCS configurations are curved by 30° with respect to the x-y plane. Results shown in Figs. 12(a), 12(b) and 12(c) reveal that the major effect of changing the wavelength is on the beam widths of the emerged EM radiation. However, in the case of convex lens, the effect of changing the wavelength on the beam width and the back radiation is found to be insignificant as depicted in Figs. 12(d), 12(e) and 12(f). Nevertheless, in the case of the concave lens geometry, the effects on the beam width and the back radiation become more pronounced at 666.7 nm and 316 nm than at 461.5 nm as shown in Figs. 12(g), 12(h) and 12(i).

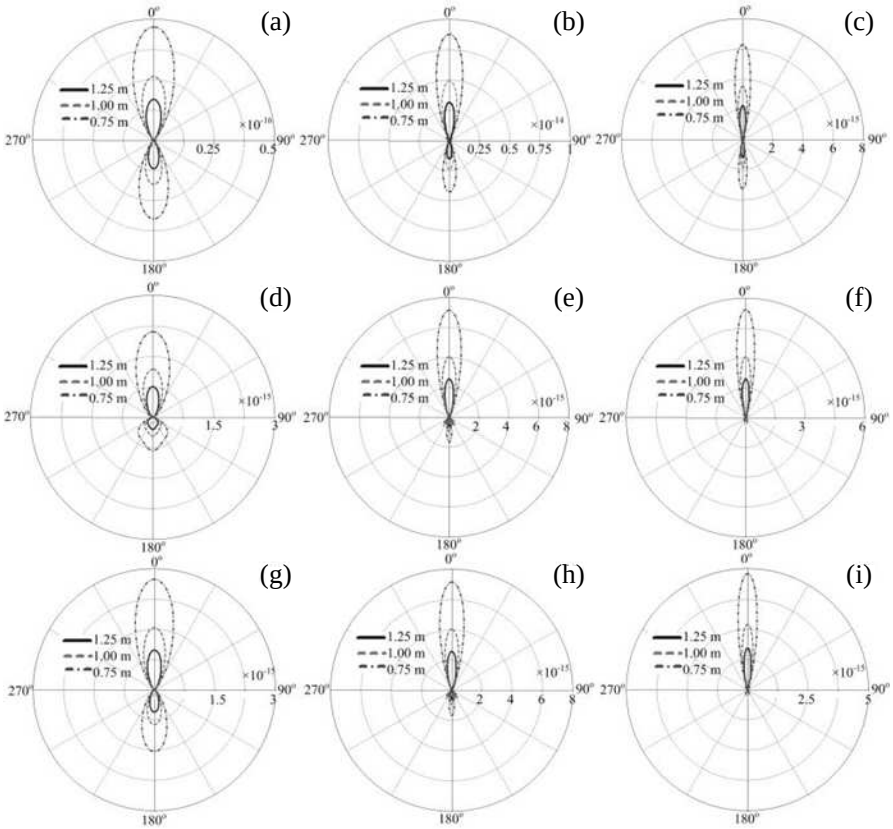

Figure 12. Power density patterns for the 9×9 NSSCS array at $\varphi = 90°$ and for wavelengths of 666.7 nm, 461.5 nm and 316 nm; (a), (b) and (c) for planar lens, (d), (e) and (f) for convex lens, (g), (h) and (i) for concave lens.

The observed differences in the performance of the proposed lenses can be further revealed by examining the fields induced on the surface of the NSSCS array as seen in Fig. 13.

The effect of increasing the size of the curved lens to 11×11 unit

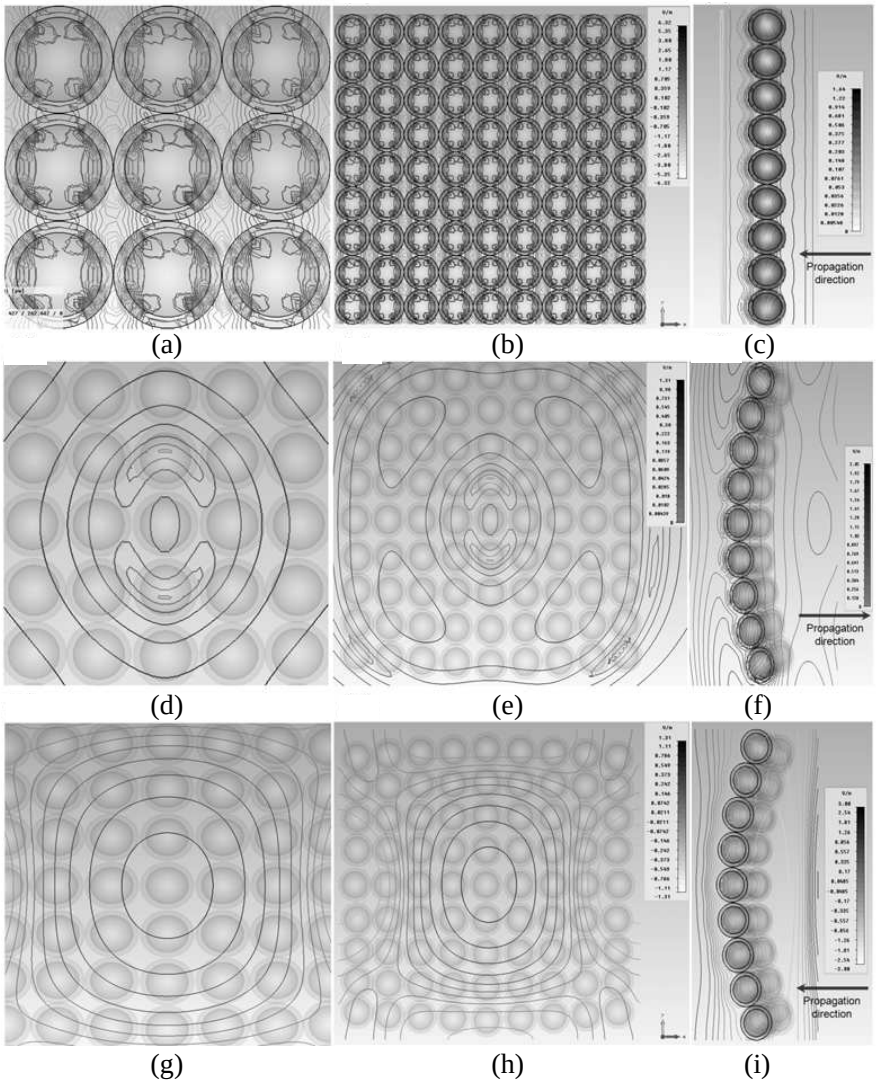

Figure 13. Field patterns induced on the surface of the 9×9 NSSCS array at 461.5 nm; (a), (b) and (c) for planar lens, (d), (e) and (f) for convex lens, (g), (h) and (i) for concave lens.

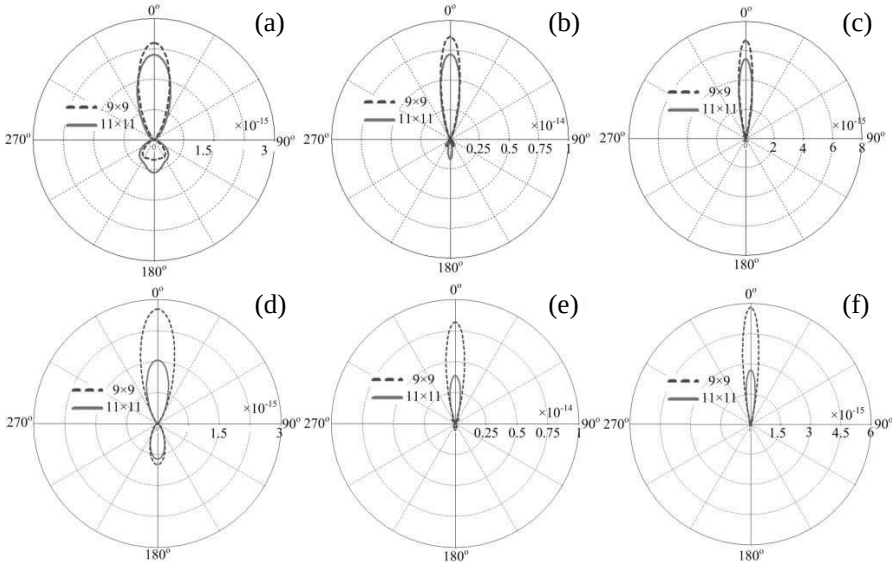

Figure 14. Power density pattern from the curved 9×9 and 11×11 lens of 9×9 and 11×11 versus $\theta = 0°$ to $360°$ at $\varphi = 90°$; (a), (b) and (c) for convex lens, (d), (e) and (f) for concave lens.

cells on the power density pattern at wavelengths of 666.7 nm, 461.5 nm and 316 nm is presented in Fig. 14. As seen as in Figs. 14(a), 14(b) and 14(c), the magnitude of the power density and the beam width of the beam emerged from the convex lens is virtually affected with changing the lens size. The magnitude of the power density pattern from the concave lens increases while the beam width of the emerged beam is almost constant as shown in Figs. 14(d), 14(e) and 14(f). In general, the back radiation is reduced by increasing the size of the NSSCS array. Moreover, the power density is increased in the case of the concave lens much more than the convex lens.

4.3. Optical Properties of the EM Beam Emerging from the Proposed Lenses

The optical properties of the EM beams emerging from the proposed lenses are characterized using an analytical formulation based on classical concepts in optics under the paraxial rays approximation [26]. The formulation is applied to show the ability of the proposed lenses in this paper to provide high focusing in the near fields with minimum beam width. Since the emerged EM beam, highly focused, shows

a circular symmetry, the use of the Gaussian beam approximation is valid. The validity is based on the asymptotic behavior of the exponential decaying in the Gaussian and Bessel beams around the beam waist W_o [26]. The optical properties are evaluated at 666.7 nm, 461.5 nm and 316 nm. These wavelengths are selected at three different loss regions as presented in Fig. 6. The beam waist is calculated from [26]

$$W_o = \frac{\lambda}{\pi\theta_o} \tag{1}$$

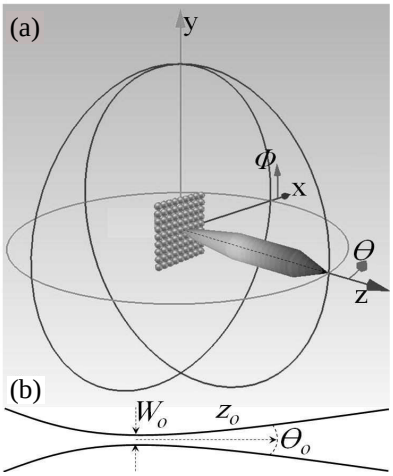

Figure 15. Conceptual diagram of Gaussian beam; (a) obtained from CST, (b) obtained from Gaussian optics.

Table 1. Properties of the emerged EM beam.

	Wavelength (nm)	$2\theta_o$ (deg.)	W_o (nm)	z_o (nm)
Flat	666.7	36.4	334.03	105.16
	461.5	20.7	406.64	225.11
	316	15.2	387.90	285.65
Convex	666.7	33.3	365.12	125.65
	461.5	20.1	418.78	238.75
	316	15.1	381.41	289.45
Concave	666.7	38.8	313.36	925.49
	461.5	23.6	356.67	173.18
	316	18.1	318.19	201.45

where θ_o, shown in Fig. 15, is the $1/e^2$ beam width. The depth of focus is calculated as

$$z_o = \frac{2\pi W_o^2}{\lambda} \tag{2}$$

In Table 1, θ_o, W_o and z_o are listed for the flat and curved lenses. The flat and convex lenses provide W_o around 400 nm for z_o about 200 nm as listed in Table 1. This property is much desired when the solar panel is positioned directly below the Fresnel lens [24]. However, the concave lens shows significant fluctuation in z_o. The beam waist versus

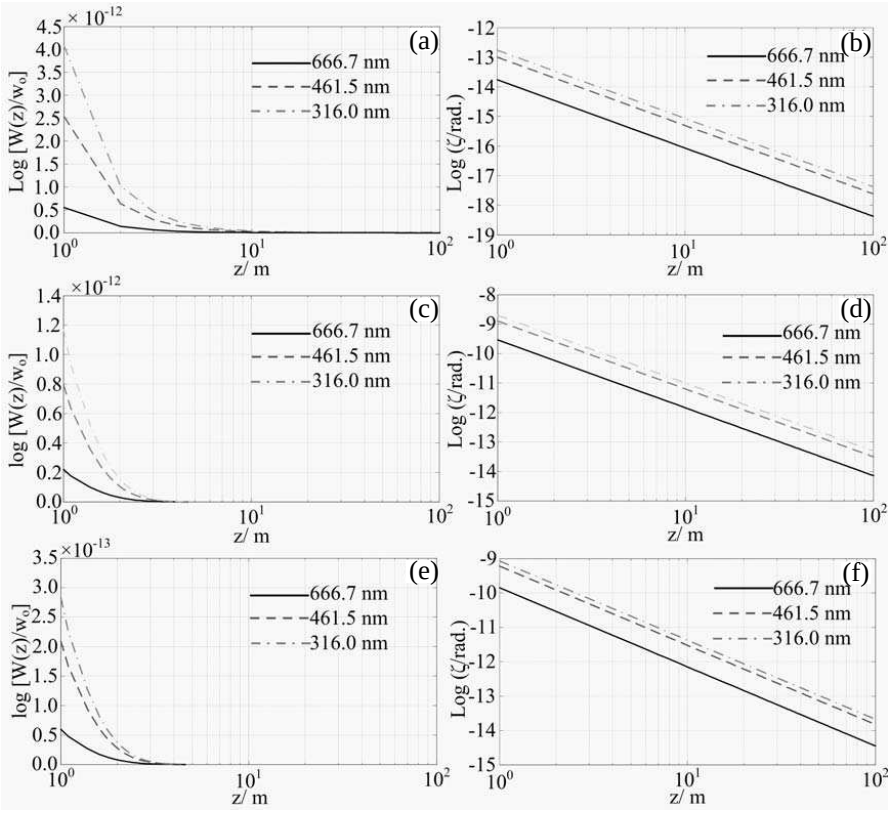

Figure 16. EM properties of the emerged beam from the proposed lenses based on 9×9 NSSCS array; (a) and (b) beam waist and phase retardation for planar lens, (c) and (d) beam waist and phase retardation for convex lens, (e) and (f) beam waist phase retardation for concave lens.

distance z can be calculated as [26]

$$W(z) = W_o \left[1 + \left(\frac{z_o}{z}\right)^2\right]^{1/2} \tag{3}$$

The phase retardation of the emerged beam at any distance z is given by

$$\varsigma(z) = \arctan\left(\frac{z_o}{z}\right) \tag{4}$$

In Fig. 16, $W(z)$ and $\varsigma(z)$ are given in log scale. It can be seen from the EM properties of the emerged beam, $W(z)$ and $\varsigma(z)$ that the flat and curved lenses provide excellent stability with respect to the propagation direction z.

5. CONCLUSION

The EM characteristics of Fresnel lenses based on a finite array of NSSCS with planar, concave and convex are reported in this paper. The EM properties of the NSSCS array are extracted from the infinite NSSCS array as FSS, MTM and EBG for the wavelength range from 0.3 µm to 300 µm. It is found the NSSCS array shows excellent transmittance over certain wavelengths, which can lead to increased coupling efficiency to solar cell panels. The real part of n_{eff} is positive over the considered wavelength range and significant losses are observed over certain wavelength bands that may lead to reduction in the power density of the EM beam emerging from the proposed lenses. It is found the NSSCS array does not have a stop band over the considered wavelength range. The optical properties of the 9×9 Fresnel lenses array are evaluated using Gaussian optical formalism at 666.7 nm, 461.5 nm and 316 nm. It is concluded that the convex design provides a virtual change in the beam widths at 666.7 nm, 461.5 nm and 316 nm. The concave design, however, provides almost constant beam widths at 666.7 nm, 461.5 nm and 316 nm with respect to the size of the proposed lenses.

ACKNOWLEDGMENT

The authors would like to thank Dr. Akhlesh Lakhtakia, Pennsylvania State University, for his helpful discussion.

REFERENCES

1. Rosenfeld, J., et al., *Averting the Next Energy Crisis: The Demand Challenge*, Vol. 12, McKinsey Global Institute, San Francisco, CA, 2009.
2. Ginley, D., M. A. Green, and R. Collins, "Solar energy conversion toward 1 Terawatt," *MRS Bull.*, Vol. 33, 355–64, 2008.
3. Singh, R., "Why silicon is and will remain the dominant photovoltaic material," *J. Nanophoton.*, Vol. 3, 032503, 2009.
4. Green, M. A., *High Efficiency Silicon Solar Cells*, Trans. Tech. Publications, VT, Brookfield, 1987.
5. Jung, Y. J., D. Park, S. Koo, S. Yu, and N. Park, "Metal slit array Fresnel lens for wavelength-scale optical coupling to nano-photonic waveguides," *Optics Express*, Vol. 17, No. 21, Oct. 2009.
6. Chen, Q. and D. R. S. Cumming, "Visible light focusing demonstrated by plasmonic lenses based on nano-slits in an aluminum film," *Optics Express*, Vol. 18, No. 14, Jul. 2010.
7. Szabó, Z., G. Park, R. Hedge, and E. Li, "A unique extraction of metamaterial parameters based on Kramers-Kronig relationship," *IEEE Tran. Micr. Theory and Tech.*, Vol. 58, No. 10, 451–461, 2010.
8. Hamam, R. E., M. Ibanescu, S. G. Johnson, J. D. Joannopoulos, and M. Soljacic, "Broadband super-collimation in a hybrid photonic crystal structure," *Opt. Soc. of Am. A*, Vol. 17, No. 10, 1–10, 2009.
9. Chen, X., T. M. Grzegorczyk, B. Wu, J. Pacheco, and J. Kong, "Robust method to retrieve the constitutive effective parameters of metamaterials," *Phy. Rev. B*, Vol. 70, 2004.
10. Tserkezis, C. and N. Stefanou, "Retrieving local effective constitutive parameters for anisotropic photonic crystals," *Phy. Rev. B*, Vo. 81, 2010.
11. Alù, A. and N. Engheta, "Input impedance, nanocircuit loading and radiation tuning of optical nanoantennas," *Phy. Rev. Lett.*, Vol. 101, 1–4, 2008.
12. Alù, A. and N. Engheta, "Enhanced directivity from subwavelength infrared/optical nano-antennas loaded with plasmonic materials or metamaterials," *IEEE Trans. Ant. and Prop.*, Vol. 55, No. 11, 2007.
13. Alù, A. and N. Engheta, "Sub-wavelength focusing and negative refraction along positive-index and negative-index plasmonic nano-transmission lines and nano-layers," *IEEE Ant. and Prop.*

Soci. Int. Symp., Vol. 35, 2005.

14. Maldovan, M. and E. L. Thomas, "Diamond-structured photonic crystals," *Nat. Mat.*, Vol. 3, 593–600, 2004.
15. Russella, P. S. J., S. Tredwella, and P. J. Roberts, "Full photonic bandgaps and spontaneous emission control in 1D multilayer dielectric structures," *Opt. Commun.*, Vol. 160, 66–71, 1999.
16. Chigrin, D. N., A. V. Lavrinenko, D. A. Yarotsky, and S. V. Gaponenko, "Observation of total omnidirectional reflection from a one-dimensional dielectric lattice," *Appl. Phy. A: Mat. Sci. and Proc.*, Vol. 68, 25–28, 1999.
17. Yablonovitch, E., "Inhibited spontaneous emission in solid-state physics and electronics," *Phy. Rev. Lett.*, Vol. 58, No. 20, 2059–2062, 1987.
18. Joannopoulos, J. D., S. G. Johnson, J. N. Winn, and R. D. Meade, *Photonic Crystals: Molding the Flow of Light*, 2nd Edition, Princeton University Press, 2008.
19. Caloz, C. and T. Itoh, "EM metamaterials: Transmission line theory and microwave applications," *Wiley Interscience*, John Wiley and Sons, Hoboken, New Jersey, 2006.
20. Munk, B. A., *Frequency Selective Surfaces: Theory and Design*, John Wiley and Sons, Hoboken, New Jersey, 2000.
21. Wu, T. K. and S. W. Lee, "Multiband frequency selective surface with multiring patch elements," *IEEE Trans. Ant. and Prop.*, Vol. 42, No. 11, 1484–1490, 1994.
22. Bardi, I., R. Remski, D. Perry, and Z. Cendes, "Plane wave scattering from frequency selective surfaces by the finite element method," *COMPUMAG Conf. Proc.*, Evian France, 2001.
23. Computer Simulation Technology/ Microwave Studio CST MWS, 2010, http://www.cst.com.
24. Chiadini, F., V. Fiumara, A. Scaglione, and A. Lakhtakia, "Simulation and analysis of prismatic bioinspired compound lenses for solar cells," *IOP Bio. and Biom.*, Vol. 5, No. 026002, 1–10, 2010.
25. Brillouin, L., *Wave Propagation in Periodic Structures: Electric Filters and Crystal Lattices*, McGraw-Hill, 1946.
26. Saleh, B. A. E. and M. Carl Teich, "Fundamentals of photonics," *Wiley Series in Pure App. Opti.*, John Wiley and Sons, Hoboken, New Jersey, 2007.